The Astrophysical Journal, 787:54 (9pp), 2014 May 20 doi:10.1088/0004-637X/787/1/54

DISTANCE AND PROPER MOTION MEASUREMENT OF WATER MASERS IN SHARPLESS 269 IRS 2w

Y. Asaki[1,2], H. Imai[3], A. M. Sobolev[4], and S. Yu. Parfenov[4]
[1] Institute of Space and Astronautical Science, 3-1-1 Yoshinodai, Chuou, Sagamihara, Kanagawa 252-5210, Japan; asaki@vsop.isas.jaxa.jp
[2] Department of Space and Astronautical Science, School of Physical Sciences, The Graduate University for Advanced Studies (SOKENDAI), 3-1-1 Yoshinodai, Chuou, Sagamihara, Kanagawa 252-5210, Japan
[3] Department of Physics and Astronomy, Graduate School of Science and Engineering, Kagoshima University, 1-21-35 Korimoto, Kagoshima 890-0065, Japan; hiroimai@sci.kagoshima-u.ac.jp
[4] Ural Federal University, Lenin Avenue 51, Ekaterinburg 620000, Russia; Andrej.Sobolev@urfu.ru, Sergey.Parfenov@urfu.ru
Received 2013 November 8; accepted 2014 April 3; published 2014 May 2

ABSTRACT

We present astrometric analysis of archival data of water masers in the star-forming region Sharpless 269 (S269) IRS 2w, observed with the VLBI Exploration of Radio Astrometry. An annual parallax of one of the bright maser features in this region was previously reported to be 0.189 ± 0.008 milliarcsecond (mas) using part of the same archival data as we used. However, we found that this maser feature is not the best to represent the annual parallax to S269 IRS 2w because the morphology is remarkably elongated in the east–west direction. For this study we have selected another maser feature showing simpler morphology. This makes the new annual parallax estimate more credible. Our newly obtained annual parallax is 0.247 ± 0.034 mas, corresponding to $4.05^{+0.65}_{-0.49}$ kpc. This value is well consistent with the 3.7–3.8 kpc obtained using the kinematic distance estimates and photometric distance modulus. We considered two hypotheses for the water-maser spatial distribution, a bipolar outflow and an expanding ring, in a kinematic model fitting analysis with a radially expanding flow. At this stage, any conclusions about the systemic proper motion could not be drawn from the kinematic analysis. Alternatively, we evaluated the mean proper motion to be $(0.39 \pm 0.92, -1.27 \pm 0.90)$ mas yr^{-1} eastward and northward, respectively, from the obtained proper motions of the detected water-maser features. The newly obtained annual parallax and mean proper motion give the peculiar motion of S269 IRS 2w to be (U_s, V_s, W_s) of $(8 \pm 6, -21 \pm 17, 1 \pm 18)$ km s^{-1}.

Key words: Galaxy: kinematics and dynamics – Galaxy: structure – masers – stars: formation

1. INTRODUCTION

Sharpless 269 (hereafter S269) is one of several H_{II} regions in the outer Galaxy. Astrophysical masers in quantum transitions of water molecules have been detected in one of the compact infrared sources, IRS 2w (Lo & Burke 1973; Genzel & Downes 1977). The water masers were monitored from 2004 to 2006 with the VLBI Exploration of Radio Astrometry (VERA) of the National Astronomical Observatory of Japan (NAOJ) to obtain the annual parallax. A sharp-peaked spectrum at V_{LSR} of 19.7 km s^{-1} was observed at the position of S269 IRS 2w, and the annual parallax of the emission was reported to be 0.189 ± 0.008 mas using model fitting for the eastward sinusoidal motion, corresponding to $5.28^{+0.24}_{-0.22}$ kpc (Honma et al. 2007, hereafter H2007).

However, this value is considerably higher than distance estimates obtained using other methods. For example, kinematic distance estimates based on the radial velocity of CO molecules provided value of 3.7 kpc (see, Wouterloot & Brand 1989). The latest kinematic distance estimated by Xu et al. (2009) yielded 3.7 kpc using the previously adopted values of galactic rotation parameters and 3.0 kpc using the values improved by Reid et al. (2009). This estimate was based on the radial velocity of the CS(2–1) molecular radio line which traces dense cores associated with H_{II} regions (Bronfman et al. 1996). Although kinematic distance estimates are uncertain in general, they considerably exceed values of the parallax measurements, especially in the outer Galaxy, and S269 was the only significant exclusion from this rule (Reid et al. 2009). Another independent method of the distance estimate based on a distance modulus of the luminous star from the S269 stellar cluster gives 3.8 kpc (Moffat et al. 1979). Therefore, H2007's value is 40%–80% larger than all the above distance estimates, and thus there exists an unusually large discrepancy.

Another aspect which we have to carefully consider for S269 is its three-dimensional (3D) motion in the Milky Way. H2007 calculated the 3D motion from the absolute proper motion and radial velocity of the maser emission. They suggested that S269 has a very small peculiar motion with respect to a Milky Way flat rotation curve. On the other hand, Miyoshi et al. (2012, hereafter M2012) showed, from the same data as H2007, that the water-maser emissions of S269 IRS 2w are widely distributed in space and radial velocity, and have various proper motions. A systemic proper motion of S269 can be different from the absolute proper motion of the single maser emission because it may be a part of a complicated internal motion such as an outflow with a typical speed of a few tens of km s^{-1} from a massive protostar. It is worthwhile to reanalyze the archival data to intensively inspect whether S269 is really in line with the Galactic rotation by imaging a wide area of the maser emitting region.

In order to revisit the distance to S269 and its 3D motion, we extensively analyzed the VERA archival data, a part of which was already published by H2007 and M2012, including those from the follow-up observations. We describe the VERA monitoring program of S269 IRS 2w in Section 2. The data reduction procedure is presented in Section 3. Our astrometric analysis results are described in Section 4. We discuss the systemic proper motion and the 3D motion of S269 IRS 2w in Section 5, and summarize this study in Section 6. We often refer to results of a specific epoch observation (2005 March 14, or "epoch C") to compare our data reduction process with that previously reported by H2007. In this paper, we adopted a line-of-sight systemic velocity of 17.7 km s^{-1} and its standard deviation of 3.6 km s^{-1} determined from CO molecular

Table 1
Epochs of the S269 IRS 2w Astrometric Monitoring Observations

Epoch	Date	Time Range (UTC)
A[a]	2004 Nov 18	12:46–21:25
B[a]	2005 Jan 26	08:48–17:32
C[a]	2005 Mar 14	05:18–14:02
D[a]	2005 May 14	01:16–10:02
E[a]	2005 Sep 23	16:46–01:32
F[a]	2005 Nov 22	12:36–21:22
G	2005 Dec 23	10:36–19:22
H[b]	2006 Mar 6	05:56–14:42
I[b]	2006 May 13	01:26–10:12
J[b]	2006 Jul 22	20:57–05:42
K[b]	2006 Aug 7	19:56–04:42
L[b]	2006 Sep 7	07:56–02:42
M[b]	2006 Oct 16	15:26–00:12
N[b]	2006 Nov 10	13:26–22:12

Notes.
[a] Previously reported by H2007 and M2012.
[b] The data were used not for annual parallax analysis but for proper motion analysis.

line observations (Carpenter et al. 1990) with the local standard of rest (LSR) defined by Kerr & Lynden-Bell (1986). Note that we discuss the 3D motion of S269 in Section 5 with respect to the solar motion reported by Schönrich et al. (2010). Hereafter, we define a maser "spot" as an emission in a single velocity channel and a maser "feature" as a group of spots observed in at least two consecutive velocity channels at a coincident or at very closely located positions (e.g., Imai et al. 2002).

2. OBSERVATIONS

VLBI phase referencing observations of S269 IRS 2w were conducted at 22.2 GHz together with a closely located continuum source, ICRF J061357.6+130645 (hereafter abbreviated to J0613+1306; Honma et al. 2000), $0\overset{\circ}{.}73$ away, and used as a positional and fringe phase reference. Fourteen observations in total were done for two years using four VERA antennas. The observing epochs are listed in Table 1. H2007 and M2012 reported their results using the first six epoch observations. At epochs B and C, there were twelve 16 MHz baseband-converter (BBC) channels with a total bandwidth of 192 MHz prepared for J0613+1306 while a single BBC channel was prepared for S269 IRS 2w. At the other epochs there were 14 BBC channels with a total bandwidth of 224 MHz prepared for J0613+1306.

Observation duration was almost 8.8 hr. Each observation was divided into several sessions of 50 minutes each, simultaneously tracking S269 IRS 2w and J0613+1306, which were separated by short-term sessions of bright calibrators (J022105.5+355613, J041437.8+053442, 3C 120, J052245.1+141529, and J053056.4+133155) in order to check the observing systems. VLBI cross-correlation was carried out for the H_2O $J_{K-K+} = 6_{16} \rightarrow 5_{23}$ maser line with the velocity spacing of 0.2107 km s^{-1} using the Mitaka FX correlator at NAOJ, Mitaka, Japan. At epochs B and C, the central 4 MHz bandwidth of S269 IRS 2w was cross-correlated while at the other epochs the central 8 MHz bandwidth was cross-correlated. The cross-correlated fringes were corrected with updated correlator models of precise delay tracking supplied by the NAOJ VLBI correlation center. The positions of the phase tracking centers of S269 IRS 2w and J0613+1306 were set as listed in Table 2 for all the epochs. In this study, we express the positions of the water masers in S269 IRS 2w with respect to its phase tracking center position.

Table 2
Phase Tracking Center Positions of the Observed Sources

	Right Ascension (J2000)	Declination (J2000)
S269 IRS 2w[a]	$06^h14^m37\overset{s}{.}03845$	$+13^\circ49'36\overset{''}{.}2200$
J0613+1306	$06^h13^m57\overset{s}{.}69276$	$+13^\circ06'45\overset{''}{.}4012$

Note. [a] This position is the origin of the S269 IRS 2w images of Figures 1–4.

3. DATA REDUCTION

3.1. Preliminary Calibration and Phase Referencing

Data reduction was conducted using the NRAO Astronomical Image Processing Software (AIPS) version 31DEC10. We first conducted amplitude calibration for all the sources, then delay calibrations for S269 IRS 2w and J0613+1306 using the bright calibrators. Second, we produced a CLEANed image of J0613+1306 for each of the epochs using AIPS IMAGR after precise delay, phase, and amplitude corrections using AIPS FRING and CALIB. CLEAN components were used to calculate J0613+1306's visibility phases of the VERA baselines to generate phase-correction data for the phase referencing by a direct phase transfer (DPT) method (Kusuno et al. 2013). The averaged peak flux density for the 14 epochs is 0.301 ± 0.077 Jy beam^{-1}. We obtained good signal-to-noise ratio of the reference source visibilities for generating the DPT data.

In order to check the validity of using J0613+1306 as the positional reference, we conducted multiple elliptical Gaussian brightness distribution fittings of the images using AIPS JMFIT, and found that there is a weak component with at most 10% of the image brightness peak, separated 0.7–1.0 mas from the core component to the north. The reference source is an active galactic nucleus (AGN), and the brightness peak position may change if relativistic AGN jets emerge and/or move. In previous studies with the Very Long Baseline Array (VLBA) at 5 GHz, multiple jet components to the north can be seen with separations of 5–30 mas from the radio core (Lazio & Cordes 1998). However, another VLBA image of J0613+1306 at 24 GHz shows a compact core as well as a plausible minor component separated ~1 mas from the brightness peak (Charlot et al. 2010), which could be identified in our VERA images. We cannot find concrete evidence that a new jet component was generated in J0613+1306 during this monitoring period. J0613+1306's visibility phase calculated from CLEAN components of the image was subtracted from the generated DPT phase data. We conducted phase referencing for S269 IRS 2w using the DPT data.

3.2. Imaging of S269 IRS 2w

Phase referencing generally reduces short-term phase fluctuations of a target source. On the other hand, the synthesis image can be more or less distorted by the phase referencing because of residual errors in the fringe phase on a timescale of several hours. To remove such a slow phase change from the target source fringe after phase referencing, we used the following procedure. We first selected a specific velocity channel of S269 IRS 2w in which strong maser emissions with a simple structure could be detected. Second, we made an initial CLEANed image of the velocity channel. Third, we performed

fringe-fitting using AIPS FRING for the velocity channel with a solution interval of 16 minutes. In this stage, the CLEAN components were referred to a source model in the fringe-fitting to remove the visibility phase from the FRING solutions. We fitted the obtained solutions with third-order polynomials and applied the fitted polynomials to all the velocity channels of the S269 IRS 2w fringe data to improve the image quality. The same polynomials were also applied to the J0613+1306 fringe data, and the brightness distribution of J0613+1306 was re-imaged. We referred to the peak position of the re-imaged map as the positional reference for the astrometry of S269 IRS 2w.

Note that the absolute positions of the masers are still available after this procedure because, if this procedure slightly changes the positions of the masers from those of the initial CLEANed image, the same positional shift is inevitably induced in the reference source by applying the same polynomials. This procedure led to not only an improvement of the S269 IRS 2w image quality, but also to a distortion of the J0613+1306 image. Because we obtained a number of maser emissions in the star-forming region while there is only one component in the reference source, this procedure greatly improved efficiencies in determining the absolute positions of the maser spots. Nevertheless, we recognized large phase offsets in AIPS FRING solutions at epochs H to L, and N, which distorted the reference source image by applying the fitted polynomials and produced clear astrometric outliers. Hereafter, we refer to epochs A to G, and M as "available epochs" for annual parallax analysis, and to epochs H to L, and N as "discarded epochs."

3.3. Astrometric Accuracy

In the phase referencing, a relative position error of the target source with respect to the reference source position includes an unexpected peak position shift due to inaccuracies in the VLBI correlator model for the pair S269 IRS 2w and J0613+1306. Hereafter we refer to the relative position error due to the inaccuracies of the VLBI correlator model as an astrometric error. Let us evaluate the expectation of the astrometric error for the pair of sources by Monte–Carlo phase referencing observation simulations using a VLBI observation simulator, Astronomical Radio Interferometer Simulator (Asaki et al. 2007; Rioja et al. 2012), as described by Asaki et al. (2010). In the simulations we assumed the flux densities of S269 IRS 2w and J0613+1306 to be equivalently 10 and 0.3 Jy for the 15.6 kHz and 224 MHz bandwidths, respectively, which were determined from the observation results. The sources were assumed to be point sources. The tropospheric zenith path length error of 2 cm and other parameters were set as suggested for VERA observations (Honma et al. 2010). The resulting standard deviation of the astrometric error in our observation simulations is 26 and 49 μas eastward and northward, respectively. These values are utilized in the annual parallax analysis and diagnostic morphology error estimations described in Section 4.3.

4. RESULTS

4.1. Spatial Distribution of Water Masers of S269 IRS 2w

We produced a 16,384 × 16,384 pixel image cube with a 0.12 mas pixel size (1966 × 1966 square mas) for the LSR velocity ($V_{\rm LSR}$) range of 4–22 km s^{-1} with a velocity channel width of 0.2107 km s^{-1}. We conducted elliptical Gaussian brightness distribution fitting for each of the detected maser spots using AIPS JMFIT. We identified maser spots through the 14 epochs whose peak was detected to be brighter by a factor of seven or more than the image root-mean-square (rms) noise. Because there are a number of spots detected only at a single epoch, we selected 90 spots out of them which are detected at least at two epochs out of the available epochs, and/or at least at three out of all the epochs at the same velocity channel in order to make more confident detection. We finally identified 28 maser features from the 90 maser spots. Figure 1 shows the spatial distribution of the water-maser features. We labeled the maser feature groups, in which maser features are closely located to each other, as groups 1–6, from the most northeastern to the most southwestern one, as shown in Figure 1. Table 3 lists the maser feature group ID, feature ID, radial velocity, epoch when the brightness maximum, and the maximum brightness value of the 90 maser spots.

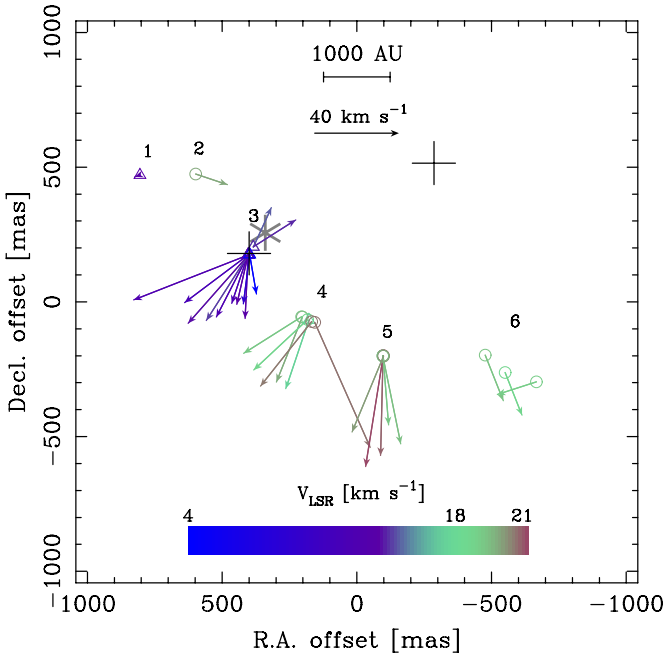

Figure 1. Spatial distribution and absolute proper motions of the water-maser features in S269 IRS 2w. Open circles and triangles represent red- and blueshifted features with respect to the systemic velocity of S269. The numbers in the plot represent the maser feature groups identified by the authors. The crosses show the assumed dynamical center discussed in Section 5. The gray asterisk represents the position of the 2MASS point source 2MASS J06143706+1349364.

We confirmed that the maser sources are widely distributed within a 1 arcsec area as reported by M2012. Comparing our images with those in M2012, the number of detected maser spots is much smaller because we excluded image components that were not convincingly recognized to be true by visual inspection. Migenes et al. (1999) found four groups of water-maser spots with $V_{\rm LSR}$ = 16.1, 17.3, 19.4, and 20.7 km s^{-1}. We identified the maser groups with $V_{\rm LSR}$ = 19.4 and 16.1 km s^{-1} as those involved in our maser feature groups 2 and 4, respectively. We found that the maser group with $V_{\rm LSR}$ = 20.7 km s^{-1} is located 100 mas north of our maser feature group 5, but could not identify the maser group with $V_{\rm LSR}$ = 17.3 km s^{-1}.

4.2. Individual Images of Water-maser Spots

Figure 2 shows a synthesized image of one of the brightest maser spots with $V_{\rm LSR}$ = 19.7 km s^{-1} in maser feature group 2 (maser spot ID 6 in Table 3) at epoch C which has been

Table 3
Positions and Absolute Proper Motions of Water-maser Spots in S269 IRS 2w

Spot ID (Group ID-Feature ID)	$\Delta\alpha_A \cos\delta$[a] (mas)	$\Delta\delta_A$[a] (mas)	$V_{\rm LSR}$ (km s^{-1})	$F_{\rm max}$[b] (Jy beam^{-1})	Epoch of the peak	$\mu_\alpha \cos\delta$ (mas yr^{-1})	μ_δ (mas yr^{-1})
1(1-a)	805.11 ± 0.03	470.31 ± 0.02	13.6	2.0	I	0.203 ± 0.020	0.055 ± 0.016
2(1-a)	805.30 ± 0.03	470.59 ± 0.02	13.4	2.5	H	0.042 ± 0.019	−0.140 ± 0.015
3(2-a)	598.22 ± 0.02	474.58 ± 0.01	20.3	2.6	C	−0.875 ± 0.015	−0.235 ± 0.010
4(2-a)	598.15 ± 0.01	474.58 ± 0.01	20.1	8.4	D	−0.776 ± 0.010	−0.225 ± 0.008
5(2-a)	598.08 ± 0.01	474.57 ± 0.01	19.9	53.9	D	−0.739 ± 0.008	−0.252 ± 0.007
6(2-a)	597.92 ± 0.01	474.54 ± 0.01	19.7	109.0	C	−0.738 ± 0.008	−0.249 ± 0.007
7(2-a)	597.78 ± 0.01	474.52 ± 0.01	19.5	82.5	C	−0.718 ± 0.008	−0.246 ± 0.007
8(2-a)	597.80 ± 0.01	474.51 ± 0.01	19.3	27.8	B	−0.725 ± 0.009	−0.260 ± 0.007
9(2-a)	597.80 ± 0.01	474.57 ± 0.01	19.1	4.7	B	−0.747 ± 0.013	−0.313 ± 0.010
10(2-a)	598.20 ± 0.02	474.60 ± 0.01	18.9	1.7	C	−0.934 ± 0.028	−0.312 ± 0.016
11(3-a)	383.94 ± 0.02	203.53 ± 0.02	14.7	1.1	F	−0.443 ± 0.024	0.976 ± 0.024
12(3-b)	384.69 ± 0.03	203.86 ± 0.03	15.1	1.3	D	−1.083 ± 0.030	0.700 ± 0.031
13(3-b)	384.45 ± 0.02	203.88 ± 0.02	14.4	1.7	F	−0.932 ± 0.022	0.622 ± 0.021
14(3-b)	384.60 ± 0.02	203.78 ± 0.02	14.2	2.7	B	−1.067 ± 0.021	0.732 ± 0.021
15(3-b)	384.61 ± 0.02	203.81 ± 0.02	14.0	3.7	B	−1.071 ± 0.021	0.700 ± 0.021
16(3-b)	384.62 ± 0.02	203.78 ± 0.02	13.8	3.3	B	−1.061 ± 0.023	0.705 ± 0.025
17(3-b)	384.62 ± 0.02	203.82 ± 0.02	13.6	2.2	B	−1.034 ± 0.025	0.626 ± 0.026
18(3-b)	384.66 ± 0.02	203.80 ± 0.02	13.4	1.8	G	−1.087 ± 0.025	0.596 ± 0.026
19(3-c)	404.40 ± 0.02	173.75 ± 0.02	12.3	4.4	M	0.348 ± 0.011	−1.260 ± 0.010
20(3-c)	404.21 ± 0.02	173.50 ± 0.02	12.1	3.0	M	0.453 ± 0.012	−1.121 ± 0.011
21(3-d)	403.50 ± 0.02	173.92 ± 0.02	13.6	5.2	N	0.280 ± 0.011	−1.223 ± 0.010
22(3-e)	403.59 ± 0.02	174.26 ± 0.02	12.5	3.2	M	0.785 ± 0.012	−1.535 ± 0.011
23(3-f)	403.14 ± 0.02	174.73 ± 0.02	13.8	4.4	G	0.083 ± 0.018	−1.732 ± 0.018
24(3-f)	403.29 ± 0.02	174.47 ± 0.02	13.6	2.4	G	−0.035 ± 0.020	−1.483 ± 0.019
25(3-f)	403.18 ± 0.02	174.50 ± 0.02	13.4	2.5	D	0.186 ± 0.024	−1.512 ± 0.022
26(3-g)	402.61 ± 0.02	174.49 ± 0.02	14.7	4.7	H	0.902 ± 0.011	−1.627 ± 0.009
27(3-g)	402.18 ± 0.01	174.51 ± 0.01	14.4	7.0	L	1.113 ± 0.009	−1.613 ± 0.008
28(3-g)	402.23 ± 0.01	174.49 ± 0.01	14.2	9.7	L	1.057 ± 0.008	−1.584 ± 0.007
29(3-g)	402.13 ± 0.01	174.63 ± 0.01	14.0	9.2	M	1.088 ± 0.008	−1.655 ± 0.007
30(3-h)	401.99 ± 0.02	174.78 ± 0.02	12.3	8.8	D	1.887 ± 0.045	−1.438 ± 0.043
31(3-h)	402.27 ± 0.02	174.68 ± 0.02	12.1	7.8	C	1.559 ± 0.074	−1.016 ± 0.072
32(3-h)	402.26 ± 0.02	174.85 ± 0.02	11.9	6.4	C	1.402 ± 0.050	−1.520 ± 0.048
33(3-h)	402.36 ± 0.02	174.69 ± 0.02	11.7	3.8	C	1.226 ± 0.078	−0.950 ± 0.076
34(3-h)	402.20 ± 0.03	174.71 ± 0.03	11.5	2.0	C	1.812 ± 0.093	−0.971 ± 0.090
35(3-i)	401.29 ± 0.02	174.74 ± 0.02	13.8	7.7	M	1.497 ± 0.010	−1.692 ± 0.009
36(3-j)	400.80 ± 0.02	174.81 ± 0.02	12.8	1.7	A	2.886 ± 0.109	−1.285 ± 0.094
37(3-j)	400.75 ± 0.02	174.78 ± 0.02	12.5	2.2	A	2.799 ± 0.099	−0.946 ± 0.088
38(3-k)	397.29 ± 0.02	175.05 ± 0.01	10.9	3.3	F	0.208 ± 0.014	−0.950 ± 0.014
39(3-k)	397.25 ± 0.01	175.27 ± 0.01	10.7	7.7	F	0.242 ± 0.011	−1.148 ± 0.010
40(3-k)	397.34 ± 0.01	175.37 ± 0.01	10.4	10.9	F	0.180 ± 0.011	−1.203 ± 0.009
41(3-k)	397.45 ± 0.01	175.28 ± 0.01	10.2	9.7	H	0.110 ± 0.010	−1.107 ± 0.009
42(3-k)	397.53 ± 0.01	175.39 ± 0.01	10.0	6.0	H	0.110 ± 0.011	−1.193 ± 0.010
43(3-k)	397.65 ± 0.01	175.32 ± 0.01	9.8	4.6	F	0.129 ± 0.013	−1.138 ± 0.012
44(3-k)	397.71 ± 0.01	175.35 ± 0.01	9.6	7.8	F	0.159 ± 0.013	−1.196 ± 0.012
45(3-k)	397.75 ± 0.01	175.40 ± 0.01	9.4	13.3	F	0.167 ± 0.013	−1.240 ± 0.012
46(3-k)	397.84 ± 0.01	175.40 ± 0.01	9.2	18.0	F	0.125 ± 0.013	−1.243 ± 0.012
47(3-k)	397.86 ± 0.01	175.41 ± 0.01	9.0	18.9	F	0.133 ± 0.013	−1.232 ± 0.012
48(3-k)	397.93 ± 0.01	175.38 ± 0.01	8.8	16.6	F	0.084 ± 0.013	−1.203 ± 0.012
49(3-k)	398.00 ± 0.01	175.40 ± 0.01	8.5	10.8	F	0.018 ± 0.013	−1.198 ± 0.013
50(3-k)	398.02 ± 0.01	175.48 ± 0.01	8.3	5.4	F	0.036 ± 0.014	−1.284 ± 0.013
51(3-k)	398.07 ± 0.01	175.49 ± 0.01	8.1	2.7	F	0.022 ± 0.016	−1.300 ± 0.015
52(3-k)	397.93 ± 0.02	175.52 ± 0.02	7.9	1.6	F	0.175 ± 0.020	−1.289 ± 0.019
53(3-k)	397.49 ± 0.03	175.78 ± 0.03	7.7	1.0	F	0.637 ± 0.025	−1.554 ± 0.026
54(3-l)	398.03 ± 0.03	175.70 ± 0.04	4.5	1.6	B	0.274 ± 0.134	−0.539 ± 0.172
55(3-l)	398.19 ± 0.03	175.79 ± 0.04	4.3	1.3	C	−0.429 ± 0.125	−0.753 ± 0.167
56(3-l)	398.22 ± 0.04	176.05 ± 0.05	4.1	1.0	C	−0.358 ± 0.146	−1.633 ± 0.177
57(4-a)	201.42 ± 0.02	−55.40 ± 0.02	20.1	3.6	F	1.076 ± 0.020	−2.254 ± 0.021
58(4-a)	202.09 ± 0.02	−56.34 ± 0.02	19.3	7.6	F	0.423 ± 0.015	−1.319 ± 0.015
59(4-a)	202.09 ± 0.02	−56.43 ± 0.02	19.1	2.9	E	0.433 ± 0.018	−1.245 ± 0.018
60(4-b)	204.94 ± 0.02	−55.10 ± 0.02	18.9	3.4	C	1.433 ± 0.080	−0.904 ± 0.080
61(4-c)	182.69 ± 0.02	−65.34 ± 0.02	18.4	5.3	C	1.193 ± 0.072	−1.217 ± 0.072
62(4-c)	182.61 ± 0.02	−65.29 ± 0.02	18.2	15.4	C	1.473 ± 0.069	−1.371 ± 0.069
63(4-c)	182.66 ± 0.02	−65.36 ± 0.02	18.0	18.3	C	1.322 ± 0.071	−1.159 ± 0.071
64(4-d)	178.12 ± 0.02	−67.43 ± 0.02	17.4	6.9	B	0.228 ± 0.100	−1.602 ± 0.094
65(4-d)	178.12 ± 0.02	−67.45 ± 0.02	17.2	16.7	B	0.236 ± 0.082	−1.415 ± 0.083

Table 3
(Continued)

Spot ID (Group ID-Feature ID)	$\Delta\alpha_A \cos\delta$[a] (mas)	$\Delta\delta_A$[a] (mas)	$V_{\rm LSR}$ (km s^{-1})	$F_{\rm max}$[b] (Jy beam^{-1})	Epoch of the peak	$\mu_\alpha \cos\delta$ (mas yr^{-1})	μ_δ (mas yr^{-1})
66(4-d)	178.07 ± 0.02	−67.43 ± 0.02	17.0	31.3	B	0.497 ± 0.083	−1.518 ± 0.080
67(4-d)	178.05 ± 0.02	−67.45 ± 0.02	16.8	40.1	B	0.656 ± 0.086	−1.382 ± 0.083
68(4-d)	177.94 ± 0.02	−67.22 ± 0.02	16.6	31.5	B	1.229 ± 0.097	−2.568 ± 0.100
69(4-e)	167.24 ± 0.02	−73.02 ± 0.02	20.6	3.3	C	1.446 ± 0.080	−1.443 ± 0.080
70(4-e)	167.37 ± 0.02	−72.98 ± 0.02	20.3	7.4	C	0.974 ± 0.072	−1.567 ± 0.071
71(4-e)	167.23 ± 0.02	−72.92 ± 0.02	20.1	12.0	C	1.380 ± 0.070	−1.781 ± 0.070
72(4-f)	157.51 ± 0.02	−75.97 ± 0.02	20.6	1.4	F	−1.879 ± 0.023	−3.355 ± 0.023
73(4-f)	156.31 ± 0.02	−76.55 ± 0.02	20.3	2.9	G	−0.866 ± 0.021	−2.818 ± 0.020
74(5-a)	−98.19 ± 0.02	−199.49 ± 0.02	21.0	3.2	M	0.439 ± 0.011	−2.741 ± 0.010
75(5-b)	−97.61 ± 0.02	−200.04 ± 0.02	20.8	4.1	K	0.126 ± 0.011	−2.413 ± 0.010
76(5-b)	−97.35 ± 0.02	−199.88 ± 0.02	20.6	9.1	K	0.001 ± 0.010	−2.515 ± 0.009
77(5-c)	−96.56 ± 0.02	−200.49 ± 0.02	19.1	596.0	M	−0.441 ± 0.010	−2.174 ± 0.009
78(5-d)	−97.14 ± 0.02	−201.38 ± 0.02	18.9	316.4	M	−0.136 ± 0.011	−1.698 ± 0.010
79(5-e)	−98.78 ± 0.02	−200.98 ± 0.01	20.3	21.2	K	0.799 ± 0.009	−1.927 ± 0.008
80(5-e)	−98.86 ± 0.02	−201.02 ± 0.01	20.1	44.9	K	0.844 ± 0.009	−1.904 ± 0.008
81(5-e)	−98.78 ± 0.02	−201.00 ± 0.01	19.9	67.7	M	0.793 ± 0.009	−1.916 ± 0.008
82(5-e)	−98.73 ± 0.02	−201.08 ± 0.01	19.7	236.3	M	0.756 ± 0.009	−1.874 ± 0.008
83(5-e)	−98.72 ± 0.02	−201.11 ± 0.02	19.5	485.6	M	0.743 ± 0.010	−1.851 ± 0.008
84(5-e)	−98.72 ± 0.02	−201.26 ± 0.02	19.3	652.4	M	0.728 ± 0.010	−1.768 ± 0.009
85(6-a)	−476.60 ± 0.02	−198.00 ± 0.02	19.1	1.8	E	−0.316 ± 0.017	−0.853 ± 0.017
86(6-a)	−476.38 ± 0.02	−197.39 ± 0.02	18.9	1.0	E	−0.577 ± 0.023	−1.398 ± 0.022
87(6-b)	−550.10 ± 0.02	−262.55 ± 0.02	18.4	2.4	E	−0.598 ± 0.018	−1.041 ± 0.018
88(6-b)	−550.39 ± 0.02	−262.44 ± 0.02	18.2	2.9	E	−0.328 ± 0.018	−1.144 ± 0.019
89(6-b)	−550.38 ± 0.02	−262.62 ± 0.02	18.0	1.4	E	−0.316 ± 0.022	−0.970 ± 0.021
90(6-c)	−666.42 ± 0.03	−297.23 ± 0.03	18.7	1.7	B	0.968 ± 0.119	−0.311 ± 0.108

Notes.
[a] The positions calculated at epoch A without annual parallax modulation. The origin is located at the phase tracking center position of S269 IRS 2w as listed in Table 2.
[b] The maximum value of the peak flux density during the monitoring program.

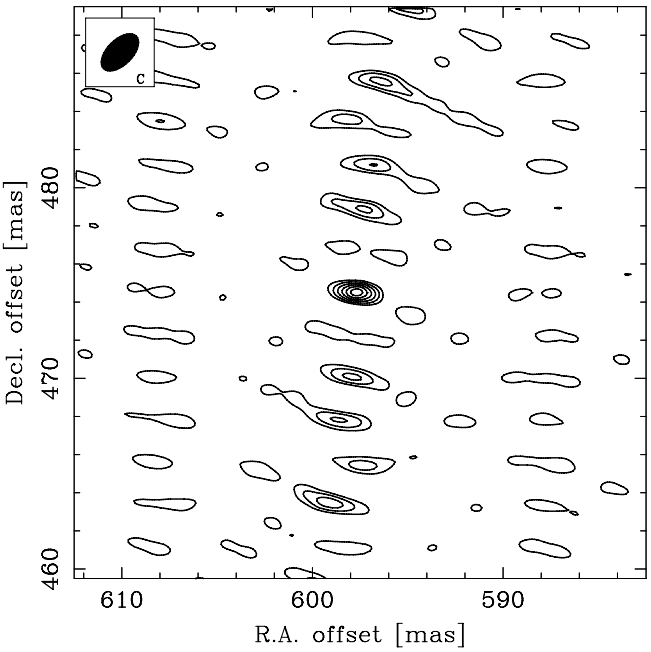

Figure 2. Brightness distribution of S269 IRS 2w around the brightest peak with $V_{\rm LSR} = 19.7\,{\rm km\,s^{-1}}$ at epoch C. The contour levels are linearly increased by 15% of the peak strength (98 Jy beam^{-1}). The synthesized beam is shown in the upper 1 × 1 square mas box.

analyzed by H2007. This maser emission has an extended structure over a few mas along the east–west direction. This maser feature may be composed of a series of emissions along this direction which cannot be distinguished by the synthesized beam. Although this maser feature has been very bright through the monitoring period, it may not be a good idea to use this feature to obtain the annual parallax because the positions may have a large uncertainty due to such an extended structure.

Figure 3 shows two examples of a trial analysis to obtain the annual parallax and proper motion for the maser spots. At this stage, we used the peak position of the brightness distribution for astrometric analysis. One example shown in Figure 3(a) is a maser spot in maser feature group 3 (maser spot ID 43 in Table 3) whose synthesis image shape is almost the same as the synthesized beam. The maser feature including this maser spot shows such an image shape, indicating that the maser emission seems to have a simple morphology. The obtained annual parallax for this single maser spot is 0.239 ± 0.043 mas by model fitting that simultaneously uses the data points in right ascension and declination (combined fitting). Another example as shown in Figure 3(b) is for the maser spot as shown in Figure 2. As already discussed above, this maser spot can be problematic in astrometric analysis because of the structure elongated east–west. Because it is difficult to separate positional changes due to time variation of an internal brightness distribution along this direction from the annual parallax eastward, an expectedly large uncertainty in measuring the annual parallax may be induced. In Section 4.3, we discuss the positional uncertainty of a maser spot using a diagnostic

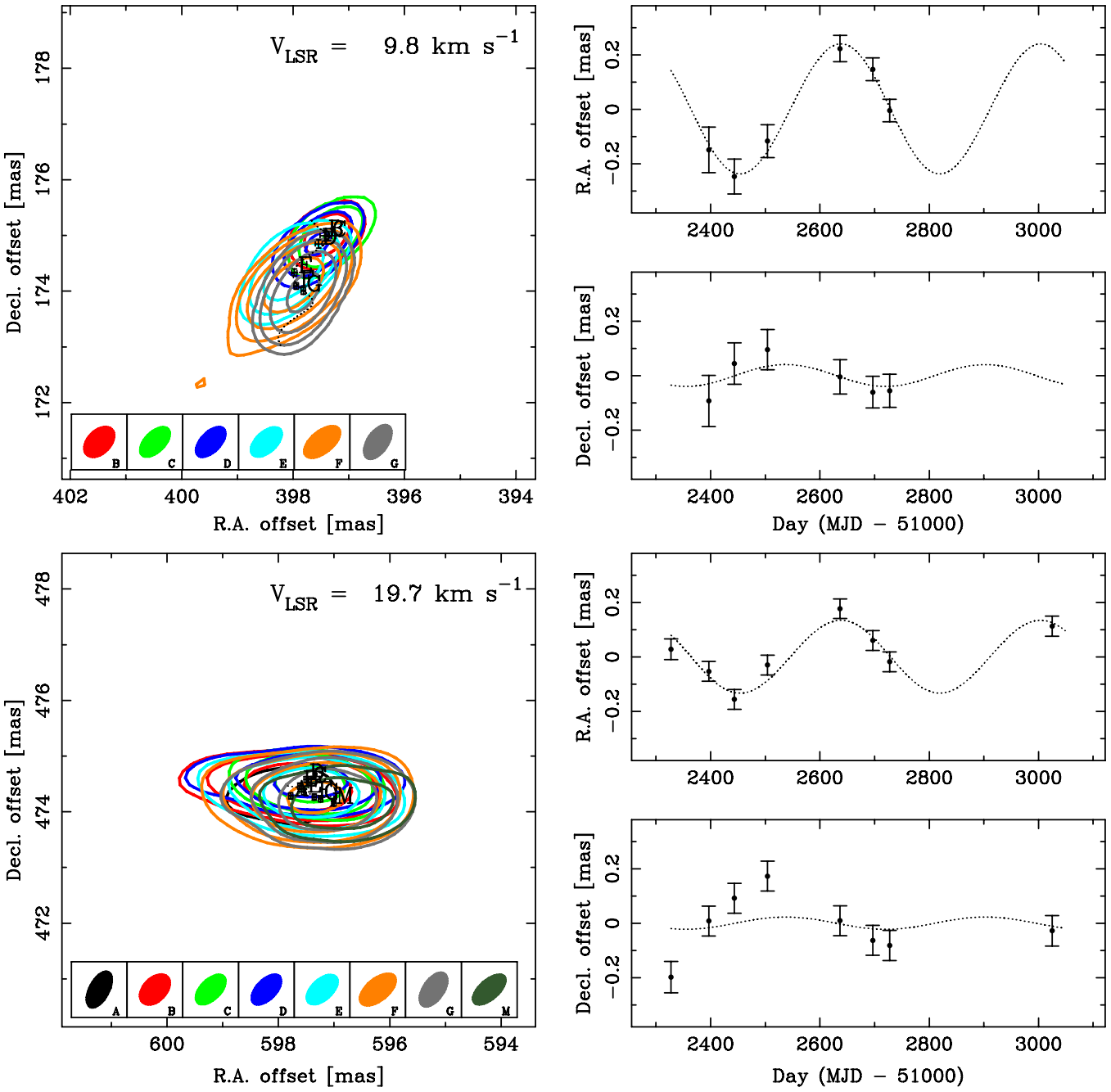

Figure 3. Astrometric analysis results of water-maser spots in S269 IRS 2w. The top three panels show the maser spot with $V_{\rm LSR} = 9.8\,{\rm km\,s^{-1}}$ in maser feature group 3. The left panel shows the image of the spots colorized for the observing epochs. The outermost contour is the 5σ noise level. The synthesized beams are shown in the bottom of the plot by 1×1 square mas. The two upper right plots show the maser spot motion eastward and northward after removing the obtained proper motion. The bottom three panels show the maser spot with $V_{\rm LSR} = 19.7\,{\rm km\,s^{-1}}$ in maser feature group 2. The outermost contour shows the 40σ noise level. The obtained annual parallaxes for the 9.8 and 19.7 $\rm km\,s^{-1}$ components are 0.239 ± 0.043 and 0.134 ± 0.022 mas, respectively.

method. This example cautions us against using such a maser spot showing complicated morphology. The obtained annual parallax for this single maser spot is 0.134 ± 0.022 mas from the combined fitting.

4.3. Annual Parallax

Following several trials of the annual parallax analysis as mentioned above, we finalized our analysis to obtain the annual parallax of S269 IRS 2w. We first selected 10 from the 90 maser spots (maser spot ID of 42–51), (1) detected in at least five out of the available epochs (A–G, and M); and (2) with the semi-major axis of the fitted elliptical Gaussian component whose direction is close to that of the synthesized beam within 30° in order to avoid maser spots with complex structures. We conducted combined fitting for all the selected maser spots simultaneously to a common annual parallax, the positions at epoch A without the annual parallax modulation (initial position), and proper motions of the individual maser spots. Details of the combined fitting are described by Kusuno et al. (2013).

We iteratively checked the residuals of the positions after subtracting the common annual parallax and individual proper motions from the spatial motions of the maser spots. The weighted rms of the residuals are 36 and 41 μas eastward

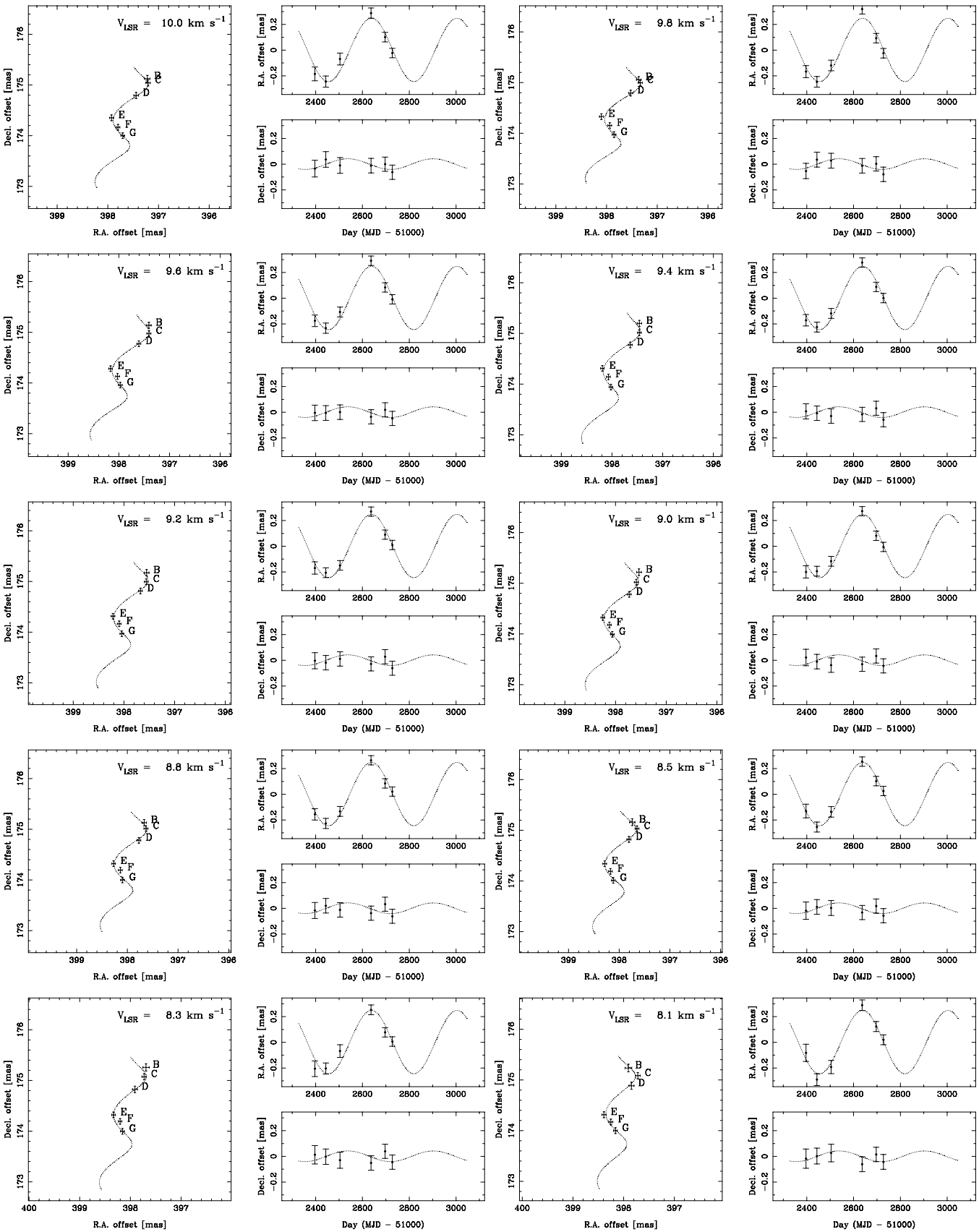

Figure 4. Same as Figure 3, but for the 10 selected maser spots for annual parallax analysis for the elliptical Gaussian components obtained with AIPS JMFIT. The positions of the maser spots are represented by the crossing points of the error bars in right ascension and declination. The common annual parallax of 0.247 mas was applied to draw the dotted lines.

and northward, respectively. Let us estimate the positional uncertainty due to the maser spot morphology (morphology error) using the following diagnostic analysis. As mentioned in Section 3.3, the astrometric error is expected to be 26 and 49 μas eastward and northward, respectively. Therefore, the position error due mainly to the morphology error is $\sqrt{36^2 - 26^2} = 25\,\mu$as eastward. On the other hand, the morphology error in declination could not be calculated because $41^2 - 49^2 < 0$. We adopted the morphology error of 25 μas for the maser spots of S269 IRS 2w. The morphology and astrometric errors were added in root-square-sum (RSS) to each of the components of the positional errors of the water-maser spots eastward and northward. Note that those additional errors make the χ^2 per degree of freedom to be close to unity. We obtained the annual parallax to be 0.247 ± 0.011 mas. The spatial motions of all the selected ten maser spots are shown in Figure 4 with the common annual parallax of 0.247 mas.

We note that all the spots are selected from the specific maser feature 3-k. In the last stage, the estimated error obtained in our annual parallax analysis for the selected maser spots should be multiplied by a factor of $\sqrt{N}$, where N is the number of selected maser spots ($N = 10$). The resultant annual parallax error is 0.034 mas, corresponding to $4.05^{+0.65}_{-0.49}$ kpc. Because this annual parallax is consistent with the kinematic distance estimates of 3.7 kpc (e.g., Wouterloot & Brand 1989; Xu et al. 2009) and the photometric distance modulus of 3.8 kpc (Moffat et al. 1979), a large discrepancy between the annual parallax and the other distance estimates for S269 is eliminated.

For information, we present the annual parallax of the maser feature 2-a, which has been analyzed by H2007. Note that this maser feature was not included in our annual parallax analysis because of its problematic morphology. We selected the three consecutive velocity channels of the brightest maser spot centered at $V_{\rm LSR} = 19.7\,{\rm km\,s^{-1}}$ as H2007 did. We applied the combined fitting to the three spots eastward and northward simultaneously while H2007 made their model fitting only for the right ascension of each of the maser spots, then averaged the three results. We obtained the annual parallax to be 0.193 ± 0.031 mas, corresponding to $5.19^{+0.98}_{-0.82}$ kpc, consistent with that of H2007. Note that the above uncertainty is a product of the combined fitting error and a factor of $\sqrt{N}$, where $N = 3$ in this case. With the diagnostic analysis mentioned above, the morphology error of the three maser spots was estimated to be 43 and 29 μas eastward and northward, respectively, for the annual parallax of 0.247 mas.

4.4. Absolute Proper Motions

We made use of all 14 epochs to obtain absolute proper motions of the maser spots. In this analysis, we have to align the maser spots detected at the discarded epochs with the maser spot map of the available epochs. In the first step, the annual parallax modulation of 0.247 mas was subtracted from the maser positions at the available epochs. We then calculated the absolute positions of maser spot ID 6 (the brightest spot in maser feature 2-a) at the discarded epochs from the preliminarily obtained initial position and the proper motion at the available epochs in Table 3. In the third step, the maser spot positions at the discarded epochs were determined in the map of the available epochs with respect to the calculated position of maser spot ID 6. We set the morphology error of all the maser spots at the discarded epochs to $\sqrt{25^2 + 43^2} = 50\,\mu$as and $\sqrt{25^2 + 29^2} = 38\,\mu$as eastward and northward, respectively, and added these to each of the positional errors in RSS. In the last step, we obtained the initial positions and absolute proper motions eastward and northward, respectively, with least square fitting for each of the 90 maser spots. The obtained parameters of the selected maser spots are listed in Table 3. Figure 1 depicts the proper motions and radial LSR velocities of 28 maser features by averaging the proper motions of the maser spots identified to be the same maser feature with a weighting of the maximum brightness as listed in Table 3.

5. DISCUSSIONS

The mean motion of the obtained proper motions, $\overline{\boldsymbol{M}}$, shows biased kinematics of $(0.39 \pm 0.92,\ -1.27 \pm 0.90)\,{\rm mas\,yr^{-1}}$, eastward and northward, respectively. To investigate a systemic proper motion of S269 IRS 2w, $\boldsymbol{M}_0$, we conducted kinematic model fitting analysis for the absolute proper motions of the water-maser features by assuming a radially expanding flow from a single originating point, $\boldsymbol{x}_0$, indicating the position of the massive young stellar object (YSO; Imai et al. 2011). We adopted the Levenburg–Marquart algorithm to search for the solutions. An additional proper motion error of $10\,{\rm mas\,yr^{-1}}$ was added to each of proper motion components eastward and northward in an RSS in order to make the χ^2 per degree of freedom almost unity.

However, we found that the resulting solutions are highly dependent on initial values of the parameters in the search. Because the location of the dynamical center is uncertain, we therefore consider constraints on the position of the originating point. Because the water masers in S269 IRS 2w form an aligned structure, there are two distinguishable major cases: with the dynamical center aligned with the masers, and with the dynamical center on the side of the maser structure. These two cases have both statistical and physical explanations, which we will describe below.

In the statistical sense, it is natural to consider locations of the dynamical center that correspond to convergence solutions. The primary candidate in this case is the best convergence solution, which is realized at $\boldsymbol{x}_0 = (400, 180)$ mas. We dare to mention that this position is close to the mean position of the water-maser spatial distribution and the near-infrared (NIR) K-band Two Micron All Sky Survey (2MASS) point source (Skrutskie et al. 2006) 2MASS J06143706+1349364 by chance, as shown in Figure 1. This 2MASS point source has an accuracy of 80 mas in the FK5 frame. Considering the difference between the FK5 frame and the ICRF, the relative positional accuracy of the point source is estimated to be ~150 mas at worst in the water-maser map. The NIR source appears only in the K-band image and is not pronounced in the J- and H-band colors. This means that the source is a deeply embedded YSO. This case suggests that the water masers are associated with a collimated bipolar outflow. A piece of evidence that the water masers trace the collimated outflow is found in the global structure around S269 IRS 2w. Eiroa et al. (1994) suggested that a Herbig–Haro object, HH 191, which is located 2.″8 to northeast of S269 IRS 2w is plausibly produced in a bow shock in a flow from S269 IRS 2w. The alignment of the water-maser features is quite similar to the direction between S269 IRS 2w and HH 191. In the case with the first candidate of $\boldsymbol{x}_0$, we obtained $\boldsymbol{M}_0 = (0.78 \pm 0.13, -1.06 \pm 0.15)\,{\rm mas\,yr^{-1}}$.

Another candidate was selected from one of the most convergent solutions, which is situated beside the maser structure at $\boldsymbol{x}_0 = (-286, 515)$ mas. This case corresponds to a

situation different from the association with the collimated outflow. One such possibility is that S269 IRS 2w's water masers may trace the cavity walls of a one-sided outflow with a rather wide opening angle, as observed in G35–0.74 (De Buizer 2006). Alternatively, the spatial distribution of the water masers may trace circumstellar structures of other nature, e.g., they can be associated with an expanding bubble (Torrelles et al. 2001) or a shock wave propagating into a rotating disk (Gallimore et al. 2003). In the case of the second candidate we obtained $\boldsymbol{M}_0 = (-0.22 \pm 0.14, -0.54 \pm 0.14)\,\mathrm{mas\,yr^{-1}}$.

At this stage, we do not have any concrete evidence of the location of the young star. In the following discussions, we obtain the 3D motion of S269 IRS 2w in the Milky Way using its mean proper motion. This proper motion shows a discrepancy with that from H2007 because they showed the analysis results only for maser feature 2-a. If we adopt the Galactocentric distance to the Sun of 8.3 ± 0.2 kpc and a flat Galactic rotation curve with rotation velocity of $239 \pm 7\,\mathrm{km\,s^{-1}}$ (Brunthaler et al. 2011), the peculiar motion of S269 IRS 2w is $(U_\mathrm{s}, V_\mathrm{s}, W_\mathrm{s}) = (8 \pm 6, -21 \pm 17, 1 \pm 18)\,\mathrm{km\,s^{-1}}$, where U_s is toward the Galactic center, V_s is toward the Galactic rotation direction, and W_s is toward the Galactic north pole at the position of the object. For the solar motion, we adopted the latest value obtained by Schönrich et al. (2010). The peculiar motion of S269 IRS 2w is prominent in the V_s component though we note that there is a rather large uncertainty because of the error in the systemic proper motion, especially in the V_s and W_s components in the case of the direction to S269 at a galactic longitude of 196.°5.

6. CONCLUSIONS

We presented the data reduction results of the VERA archival data of S269 IRS 2w, part of which was already analyzed by H2007 and M2012. The water masers ranging in LSR velocity from 4 to 21 $\mathrm{km\,s^{-1}}$ spatially distributed along the northeast–southwest direction. We obtained the annual parallax of 0.247 ± 0.034 mas for a maser feature with simple morphology residing in this star-forming region, corresponding to $4.05^{+0.65}_{-0.49}$ kpc.

In order to consider the systemic proper motion of S269 IRS 2w we presented two major hypotheses regarding the dynamical center position: within the aligned maser structure and beside it. We found that at present these two cases cannot be distinguished by reasoning based on both statistical and physical plausibility. Because we have not had clear evidence on the certain location of the source of maser excitation, we found it impossible to draw any conclusion about the systemic proper motion. Instead, using the mean motion of the water-maser proper motion, $(0.39 \pm 0.92, -1.27 \pm 0.90)\,\mathrm{mas\,yr^{-1}}$, the annual parallax of 0.247 ± 0.034 mas, and radial velocity of the S269 molecular cloud, the peculiar motion of S269 IRS 2w is estimated to be $(U_\mathrm{s}, V_\mathrm{s}, W_\mathrm{s})$ of $(8 \pm 6, -21 \pm 17, 1 \pm 18)\,\mathrm{km\,s^{-1}}$.

The authors thank an anonymous referee for careful reviews and providing valuable suggestions to improve this paper. The VERA/Mizusawa VLBI observatory is a branch of the National Astronomical Observatory of Japan, National Institutes of Nature Sciences. The authors express their deep gratitude to the VERA of NAOJ. The authors acknowledge arrangements for providing the updated VLBI correlator models by K. M. Shibata and fruitful discussions on the VERA data analysis with T. Oyama. This publication also makes use of data products from 2MASS, which is a joint project of the University of Massachusetts and the Infrared Processing and Analysis Center/California Institute of Technology, funded by the National Aeronautics and Space Administration and the National Science Foundation. This work was supported by the Japan Society for Promotion of Science (JSPS) Grant-in-Aid for Challenging Exploratory Research, grant No. 25610043. Y. A. was financially supported by the Center for the Promotion of Integrated Science of the Graduate University of Advanced Studies for this publication.

REFERENCES

Asaki, Y., Deguchi, S., Imai, H., et al. 2010, ApJ, 721, 267
Asaki, Y., Sudou, H., Kono, Y., et al. 2007, PASJ, 59, 397
Bronfman, L., Nyman, L.-Å., & May, J. 1996, A&AS, 115, 81
Brunthaler, A., Reid, M. J., Menten, K. M., et al. 2011, AN, 332, 461
Carpenter, J. M., Snell, R. L., & Schloerb, F. P. 1990, ApJ, 362, 147
Charlot, P., Boboltz, D. A., Fey, A. L., et al. 2010, AJ, 139, 1713
De Buizer, J. M. 2006, ApJL, 642, L57
Eiroa, C., Casali, M. M., Miranda, L. F., & Ortiz, E. 1994, A&A, 290, 599
Gallimore, J. F., Cool, R. J., Thornray, M. D., & McMullin, J. 2003, ApJ, 586, 306
Genzel, R., & Downes, D. 1977, A&AS, 30, 145
Honma, M., Bushimata, T., Choi, Y. K., et al. 2007, PASJ, 59, 889 (H2007)
Honma, M., Hirota, T., Jike, T., et al. 2010, PNAOJ, 13, 57
Honma, M., Oyama, T., Hachisuka, K., et al. 2000, PASJ, 52, 631
Imai, H., Deguchi, S., & Sasao, T. 2002, ApJ, 567, 971
Imai, H., Omi, R., Kurayama, T., et al. 2011, PASJ, 63, 1293
Kerr, F. J., & Lynden-Bell, D. 1986, MNRAS, 221, 1023
Kusuno, K., Asaki, Y., Imai, H., & Oyama, T. 2013, ApJ, 774, 107
Lazio, T. J. W., & Cordes, J. M. 1998, ApJS, 115, 225
Lo, K. Y., & Burk, B. F. 1973, A&A, 26, 487
Migenes, V., Horiuchi, S., Slysh, V. I., et al. 1999, ApJS, 123, 487
Miyoshi, M., Asaki, Y., Wada, K., & Imai, H. 2012, NewA, 17, 553 (M2012)
Moffat, A. F. J., Fitzgerald, M. P., & Jackson, P. D. 1979, A&AS, 38, 197
Reid, M. J., Menten, K. M., Zheng, X. W., et al. 2009, ApJ, 700, 137
Rioja, M., Dodson, R., Asaki, Y., Hartnett, J., & Tingay, S. 2012, AJ, 144, 121
Schönrich, R., Binney, J., & Dehnen, W. 2010, MNRAS, 403, 1829
Skerutskie, M. F., Cutri, R. M., Steiening, R., et al. 2006, AJ, 131, 1163
Torrelles, J. M., Patel, N. A., Gómez, J. F., et al. 2001, ApJ, 560, 853
Wouterloot, J. G. A., & Brand, J. 1989, A&AS, 80, 149
Xu, Y., Voronkov, M. A., Pandian, J. D., Li, J. J., et al. 2009, A&A, 507, 1117